RESEARCH ARTICLE

**ADVANCED
SENSOR
RESEARCH**
Open Access

www.advsensorres.com

# Fully Printed Temperature Sensor Array Comprising 625 60×60 µm² pixels

*Robert Huber, Santiago Eizaguirre, Henning Mescher, Christian Willig, Qiaoshuang Zhang, and Uli Lemmer\**

With further digitalization and automation, new applications fields require new solutions and sensors. Healthcare, soft robotics, and battery research are only three examples striving for sensor solutions capable of measuring the spatial and temporal temperature distribution of surfaces. This requires the deposition of multiple sensor pixels with a high spatial resolution on potentially flexible substrates. Printing technologies are well suited to fulfill the associated requirements of quality, speed, feature size, and costs. Combining screen printing and aerosol jet printing allows for fast large-scale processing and when needed high-precision fabrication for small features. The presented high-density temperature sensor array provides 625 sensor pixels with a size of 60×60 µm², evenly distributed over an area of 12×12 mm². The sensor is operated without encapsulation between 5 and 90 °C showing an average deviation of less than 0.5 °C. The sensor stack consists of a bottom and top electrode sandwiching a carbon black based thermistor layer. The material shows a strong negative-temperature-coefficient (NTC) effect with a sensitivity of 3.6 % °C$^{-1}$ at 5 °C. As an application example, the temperature profile induced by a laser beam is mapped with the temperature sensor array.

## 1. Introduction

Sensor technology has recently undergone great progress due to technological advances in printed electronics. New application fields and research topics such as robotics,[1–4] healthcare,[5–7] and batteries[8, 9] are demanding for tailored sensor systems. Printing technologies have proven suitable to offer easy adaptability, flexibility, and cost efficiency. Despite the given benefits and giving traditional commercial approaches competition, printing technologies still have drawbacks concerning manufacturability, miniaturization, and performance.[10, 11] These issues are addressed from three sides: First, the deposition methods are improved by continuous development of existing printing machinery and new printing functionalities. Second, it is no less important to gain full control over the ink composition and compatibility of materials, substrates, and processes. Finally, new design rules have to be implemented and optimized to reduce complexity and expenses. The constantly increasing number of publications proves the effort that is being made in the field of printed electronics.[10, 12]

Among environmental and industrial monitoring systems, temperature is one elementary parameter. The most prominent temperature acquisition methods are thermistors, thermocouples, and resistance temperature detectors (RTDs). While the fabrication of sensor systems with micron- and submicron structures using traditional lithographic methods is a well established standard procedure, it remains a challenging task to realize high spatial resolution sensor systems with printing technologies and methods of additive manufacturing. Recent publications on temperature sensors focus on two main aspects. First, the development of new ink formulations exhibiting high sensitivity and stability is widely studied. Poly(3,4-ethylenedioxythiophene) polystyrene sulfonate (PEDOT:PSS) and carbon nanotube compositions are particularly interesting as thermistor materials,[5, 13–16] while different particulate inks and pastes are widely used for thermocouples[17–19] and RTDs.[20–22] Second, the fabrication of temperature sensors either using improved printing methods or developing new sensor designs are in the focus of research. Therefore, screen printing and inkjet printing are commonly used for single and multi sensor arrangements. Simple designs are necessary for ink and printing competency development; therefore, the vast majority of the presented devices are based on single sensor designs. Research on sensor arrays dealing with

R. Huber, S. Eizaguirre, H. Mescher, Q. Zhang, U. Lemmer
Karlsruhe Institute for Technology
Light Technology Institute (LTI)
Engesserstrasse 13, 76131 Karlsruhe, Germany
E-mail: uli.lemmer@kit.edu
H. Mescher, U. Lemmer
Karlsruhe Institute of Technology
Institute of Microstructure Technology (IMT)
Hermann-von-Helmholtz-Platz 1, 76344 Eggenstein-Leopoldshafen, Germany
C. Willig, U. Lemmer
InnovationLab GmbH
Speyerer Str. 4, 69115 Heidelberg, Germany

**Table 1.** Overview on published data on temperature sensor arrays.

| Fabrication [Fullyprinted] | Material | Temperature range [°C] | Size [cm²] | Sensors [#] | Density [#/cm²] | Pixel size [mm²] | TCR [%/K] | Reference |
|---|---|---|---|---|---|---|---|---|
| Screen printing [Yes] | NTC ceramic composite | 40–140 | 7×13 | 414 | 4.5 | 6×6 | 4.00 | [4] |
| Inkjet/Screen printing [Yes] | Graphene PEDOT:PSS | 35–45 | 2×3 | 4 | 0.7 | 1×1 | 0.06 | [13] |
| Screen printing [Yes] | PEDOT:PSS | 20–90 | 1×1 | 100 | 100 | 0.4×0.4 | 0.09 | [26] |
| Screen printing [Yes] | CNT, PEDOT:PSS | 20–80 | 8×8 | 9 | 0.2 | 2×4 | 0.25 | [27] |
| Screen printing [Yes] | CNT polyvinyl chloride, carbon black | 18–44 | 7× 7* | 16 | 0.25* | 10× 10* | -0.15 | [28] |
| Inkjet [Yes] | PEDOT:PSS, PU dispersion | 25–80 | 6× 8* | 25 | 0.52* | 10× 12* | 0.32 | [29] |
| VLSI [No] | Silicon | 30–110 | 0.8×0.8 | 1024 | 1600 | 0.05×0.05 | <0.29 | [30] |
| Masking [No] | Graphite copolymer | 25–50 | 3.8×3.8 | 144 | 10.2 | 2×2 | NA | [31] |
| Thermal evaporation [No] | Pentacene, Ag NPs | 20–100 | 4×4 | 256 | 16.0 | 2.5×2.5 | <0.04 | [24] |
| Dispenser [No] | Graphite, PDMS | 30–110 | 4×4 | 64 | 5.3 | 1.5×1.5 | <0.29 | [32] |
| Screen printing/Aerosol jet [Yes] | Carbon black composite | 5–90 | 1.2×1.2 | 625 | 434 | 0.06×0.06 | <3.6 | **This work** |

*The values are estimated from the pictures.

multiple sensor pixel arrangements and upscaling usually focus on large scale devices or rely on non-printing methods.4, 23, 24

The combination of several sensor pixels to form a sensor matrix enables a temperature distribution to be measured over a surface which is particularly attractive for soft robotics. Emulating the perception of a human fingertip requires ≈250 sensors pixels per cm².25 Therefore, the pixel density has to be further increased by simultaneously decreasing the sensors size. Furthermore, there are applications that depend on even higher sensor densities. For example, measuring the beam profile or energy of infrared lasers above 1 μm wavelength mostly requires costly detection equipment with rare material combinations (In-GaAs, InSb, HgCdTe (MCT),...) or complex measurement methods (thermopile detectors, pyroelectric detectors,...). Offering inexpensive alternatives with similar performance could potentially be fulfilled by a 2D temperature sensor array. And finally, fabrication routes considering additive manufacturing offer ways to directly integrate sensors on any item's surface.

The intention for this work, was to develop a fully printed temperature sensor array with a high number of sensor pixels into a sensor matrix, being interesting for the above-mentioned use cases. The used thermistor material should be robust and applicable without encapsulation. Combining the well established screen printing process with high precise aerosol jet printing allows us to decrease the prototyping and manufacturing time, while maintaining high ink compatibility and precision. Using this approach we realize a sensor array of 625 pixels on an area of 12×12 mm². For comparison, **Table 1** provides an overview of published state-of-the-art temperature sensor arrays. Laser beam profiling is used to demonstrate the sensor capabilities to resolve a local temperature distribution. The sensor's sensitivity results in 3.6 % °C⁻¹ at 5 °C.

## 2. Design and Fabrication

The fully printed sensor array built as a passive matrix was printed stepwise using a Polyethylene naphthalate (PEN) foil as the substrate (**Figure 1**a). First, the surrounding connection lines were printed on a screen printer (I, see Figure 1a) with commer-

cially available silver ink. This process is well developed and allows us to fabricate large structures in a short time. The silver lines achieved this way, offer good conductivity and high scratch resilience, which is especially beneficial to be used with the flexible-printed-circuits (FPC) connectors for the readout electronics. The required sintering step was performed on a hotplate. Next, the actual sensor array was added to the connection line structure with the aerosol jet printer (II, see Figure 1a) in three independent passes. Aerosol jet printing ensures the high printing precision, which was necessary for the high sensor density in the desired size. Simultaneously, this printing technology offers an extraordinary ink compatibility and parameter control, which makes it appropriate to realize the sensor array with the required spatial resolution and quality. The first set of silver lines forming the bottom electrodes (II.1, see Figure 1a) were printed with the aerosol jet printer with a feature size of ≈ 60 μm. Decreasing the feature size also leads to a reduced heat conduction throughout the sensor array, which is desired to resolve local hot spots. Right after depositing, the silver lines were photonically sintered, which enhanced the conductivity compared to thermal sintering and rendered them less susceptible to crack formation. Second, we used a commercially available highly resistive carbon ink as thermistor material (II.2, see Figure 1a). We have chosen this material due to its strong temperature dependence. The ink was designed for screen printing, and thus required dilution to make it compatible to the aerosol jet printer. To adapt the resistance value to the application and the readout electronics, it was necessary to realize an appropriate layer thickness (approximately 3 μm). Twelve layers of the carbon ink were printed linewise on top of each other and perpendicular to the first set of silver electrodes. This number of layers was found to be a sweet spot forming a closed layer, without short circuits and thus resulting in a high yield of functional sensor pixel comprising a high layer uniformity. We took extra measures to increase the resistance value consistency among all sensor pixels: 1) The printed thermistor lines are as broad as possible (>300 μm) without forming a closed layer. Attempts to print a closed layer resulted in a distorted surface as the previously deposited liquid ink was pushed to the side by the flow push of the nozzle. Instead, we decided to print wide
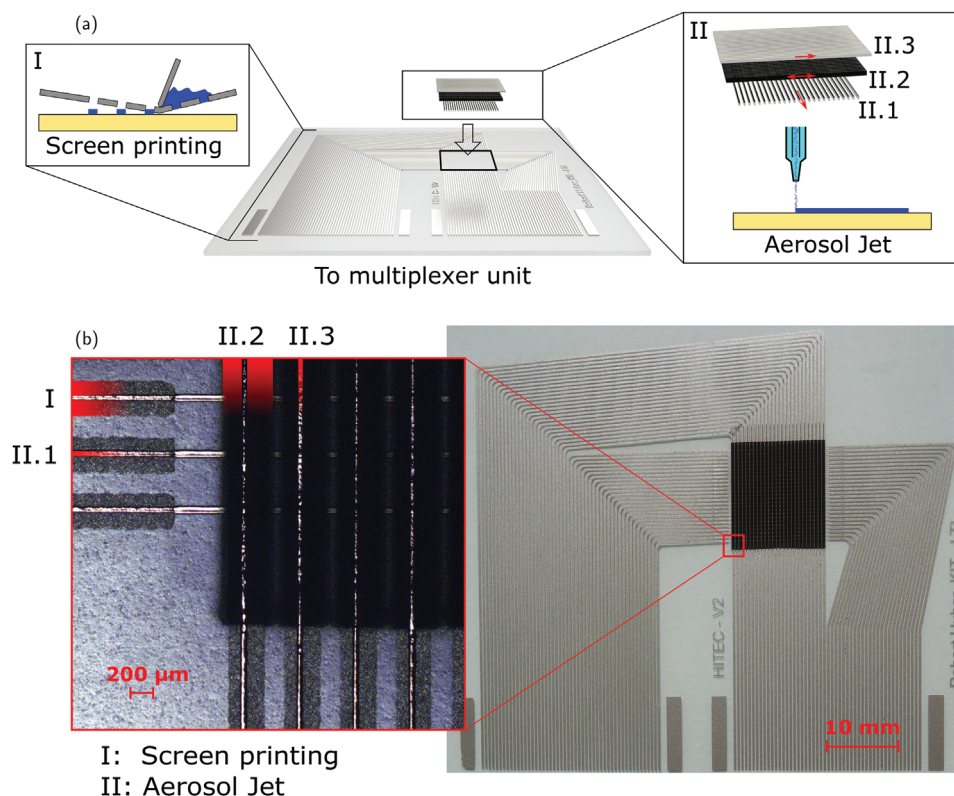
**Figure 1.** a) The fully printed temperature sensor is fabricated by combining two printing methods in a total of four steps on a PEN foil. First, I) the connection lines between sensor stack and multiplexer unit are printed via screen printing. II) An aerosol jet printing system is used for the sensor stack, which is printed stepwise from bottom to top: II.1) bottom electrode, II.2) thermistor material and II.3) top electrode. Each printing step requires a subsequent sintering or curing process. The printing direction is represented by red arrows. b) Photograph of the fully fabricated sensor array with a close-up image showing all four deposited layers marked in red.

lines, which offer a comparable evenly thick area in the middle without suffering from the effect mentioned above. This effort led to uniform resistance values throughout the sensor array. 2) Using the shutter of the aerosol jet printer can induce small pressure changes in the system, causing a tiny but noticeable fading effect on the printed lines. Therefore, each of the twelve layers and line sets were printed in one continuous meander structure. To achieve the intended structure, we aligned a polymeric mask on top of the sensor array, cropping the unnecessary parts of the meander structure in a simple lift off process, leaving the desired line structure back in place. 3) Printing several layers instead of printing one thick layer compensated for printing fluctuations (e.g., in the aerosol generation) and created a consistent material stack.

After deposition, the substrate was placed in an oven for thermal curing. Ultimately, the top silver electrodes (II.3, see Figure 1a) were fabricated similarly to the bottom electrodes. It is important to control the layer thickness of the silver line, since too thick silver layers tend to crack during flash sintering leading to a interrupted connection or, if too thin, suffering from high resistance values. Therefore, the layers were analyzed by stylus profilometry (Profilometer, DektakXT, Bruker) (Figure S1, Supporting Information) and white light interferometry (WLI) (Profilometer, ContourGT-X, Bruker) (Figure S8, Supporting Information). Both measurement methods are well suited to deter-

mine the layer dimensions. While the WLI provides an overview of the entire sensor structure, the stylus profilometer gives a detailed information about the layer texture. The measurements are in great agreement when comparing the determined layer thicknesses. All layers are between 3 and 4 µm thick with the layers in the stacks adding up in height, respectively. The screen printed silver and the thermistor material (Figure S1, Supporting Information) show a rough surface with several spikes of 1–2 µm. In contrast, the aerosol jet lines suggest a rather smooth surface structure, even though it is difficult to recognize due to the small line width and large aspect ratio. The rough texture surrounding the aerosol jet line in Figure S1b (Supporting Information) is attributed to overspray, which results from the deposition stream during the printing process.

A photo of the finalized temperature sensor array is shown in Figure 1b including a close-up view comprising all deposited layers. The cross section of two intersecting electrodes corresponds to one sensor pixel. Overall, 625 pixels of the size of 60 × 60 µm$^2$ were fabricated. The matt or glossy appearance of layers also allows conclusions to be drawn about the structure, which corresponds to the profilometric measurements. To further investigate the utilized materials and layer structure, a cross-sectional cut was provided by a combining focus ion beam (FIB) cut and scanning electron microscope SEM imaging. This generates a high contrast close-up view (Figure S2e, Supporting

**2200031 (3 of 10)**

**ADVANCED
SCIENCE NEWS**

www.advancedsciencenews.com

**ADVANCED
SENSOR
RESEARCH**

Open Access

www.advsensorres.com

Information), which goes well along with drawn texture conclusions from above and allows a cross-sectional cut of the stack structure. Figure S2a,b shows (Supporting Information) the transition area between connection lines and the sensor array. This includes the screen printing silver, thermistor, and aerosol jet silver layer with the underlying PEN substrate. The sensor pixel cross section is presented in Figure S2c,d (Supporting Information) comprising the bottom and top electrode as well as the thermistor material layer.

Some properties of the utilized inks can be deduced from the images or are stated in the manufacturer's datasheet.[33–35] The aerosol jet silver is composed of silver nanoparticles with an average size of 35 nm. During the flash sintering process, the single particles melt together and form a dense layer with voids (Figure S2, Supporting Information). On the other hand, screen printing requires a different formulation. In Figure S2a,b (Supporting Information), silver particles/flakes with the size of several tens of micrometers are visible. Although both inks are stated with a similar adhesion rating, the screen printing ink performs better and is more suitable for FPC connectors. The used thermistor material is referred to as thermoplastic-based from its manufacturer's datasheet. The ink is intended to be a highly resistive dielectric ink and designed to be blended with a second thermoplastic-carbon-composite ink. Instead of controlling the layer thickness, as done here, the resistance values can also be altered by changing the mixing ratio of the two inks. Many publications on temperature sensing deal with similar conductive polymer composites describing positive-temperature-coefficient (PTC) and/or negative-temperature-coefficient (NTC) behavior.[36–40] Commonly, these thermoplastic composite inks use a polymer matrix exhibiting a high electrical resistance. The electrical properties can be changed by adding fractions of conductive particles such as carbon or graphite derivatives to the polymer matrix. The effect is mainly influenced by the electroconductive behavior and the geometry of the filler as well as the final aggregated structure of the composite.[36] In our particular case, Figure S2c,d (Supporting Information) reveals a porous structure/matrix comprising isolated agglomerations or particles.

## 3. Results and Discussion

For characterization, the temperature sensor array was mounted into a specially designed multiplexing unit, establishing the connection between sensor sheet and source-measurement-unit (SMU). An overview of the readout setup can be found in Figure 3a. To first prove the underlying temperature dependency of the thermistor material, we measured the current–voltage (I–V) behavior at different temperatures (**Figure 2**a). The measurement was carried out on one single pixel, applying voltage sweeps between -1 and +1 V at stabilized temperature values. The data show a non-linear point symmetric NTC behavior and comprises no observable hysteresis or capacitive effects. The observed effects can be attributed to two possible effects, which may even superimpose. First, if the stack structure of metal electrode–semiconductor–metal electrode is taken into consideration, we potentially observe two Schottky barriers with opposite bias. One Schottky barrier is therefore always operated in reverse bias defining the overall I–V behavior. This can also explain the typical reverse leak current. Second, this effect is tied to the intrinsic

polymer's properties. Similar inks based on thermoplastic composites have been studied intensively in research.[36–40] Although the effect is not fully understood, the most common explanation is the relaxation of the polymer's matrix due to a lowered viscosity at elevated temperatures. This also leads to an increased mobility of the conductive carbon black particles/agglomerates and the formation of conductive chains.[41, 42] Over all, the observed symmetric curve progression fits well with the present stack structure considering the proposed assumptions. For all following measurements, the sensor was constantly operated at 500 mV. With the measured I–V behavior, it might appear beneficial to increase the voltage and take advantages of the larger current variations at the applied temperatures. This would potentially decrease the signal-to-noise ratio and lower the requirements for a stable readout electronic. Unfortunately, this goes hand-in-hand with increased power dissipation in each pixel resulting in excessive self heating. At 60 °C the power dissipation is roughly $P_{loss}(0.5\,\text{V}) = 125\,\text{nW}$ which is one sixth of the value expected if the measurement would be conducted at 1 V. In Figure 2b, the sensor is cycled between 5 and 90 °C, while the resistance of each sensor pixel was measured. The graph shows the resistance response of one pixel. All sensor pixels share a common behavior but have slightly different resistance values. This effect can be explained by small variations during the fabrication process, which are reflected, for example, in small differences in the layer thickness of the thermistor material or the cross sections of the electrodes. As described above, several measures were taken to diminish the pixel-to-pixel variations. Even after cycling the temperature for hours and multiple iterations, the sensor response was robust and reproducible, which is a basic requirement for such sensors. Similar to the I–V measurement (Figure 2a), the non-linear behavior is also observable when measuring the resistance-temperature dependency. This gets clearly visible when cycling the temperature and comparing the curve regression of the reference temperature to the measured sensor resistance. Due to the individual pixel behavior, each pixel is calibrated separately. The calibration measurement is conducted by cycling the temperature for three times between 5 and 90 °C in 5 °C steps. The resistance values for each sensor pixel at all temperature steps were recorded, along with the reference temperature from an embedded sensor in the setup. In Figure 2c the resistance values are plotted over the corresponding reference temperatures. Next, the data of each pixel was fitted with a forth order polynomial, leading to the present curve regression in the graphs. The so achieved fitting functions represents the calibration function for each sensor pixels. This function is used to convert the resistance readings back into temperature values. The sensor sensitivity expressed by the temperature coefficient of resistance (TCR) is correlated to the non-linear behavior, therefore the TCR value decreases from 3.6 % °C$^{-1}$ at 5 °C to 0.5 % °C$^{-1}$ at 90 °C. The TCR is calculated according to $\text{TCR}_{T_{rel}=5°C} = \frac{\Delta R/R}{\Delta T}$. In Figure 2c, we observed a small hysteresis effect, which is affected by whether the sensor is heated or cooled. The effect becomes smaller for higher temperatures and could possibly be compensated if the temperature history is also taken into account when converting the readings into temperature values. In this context, the long-term stability was further investigated by conducting a measurement of a single pixel over several days at a fixed temperature (Figure S3, Supporting Information). During the measurement, we found a
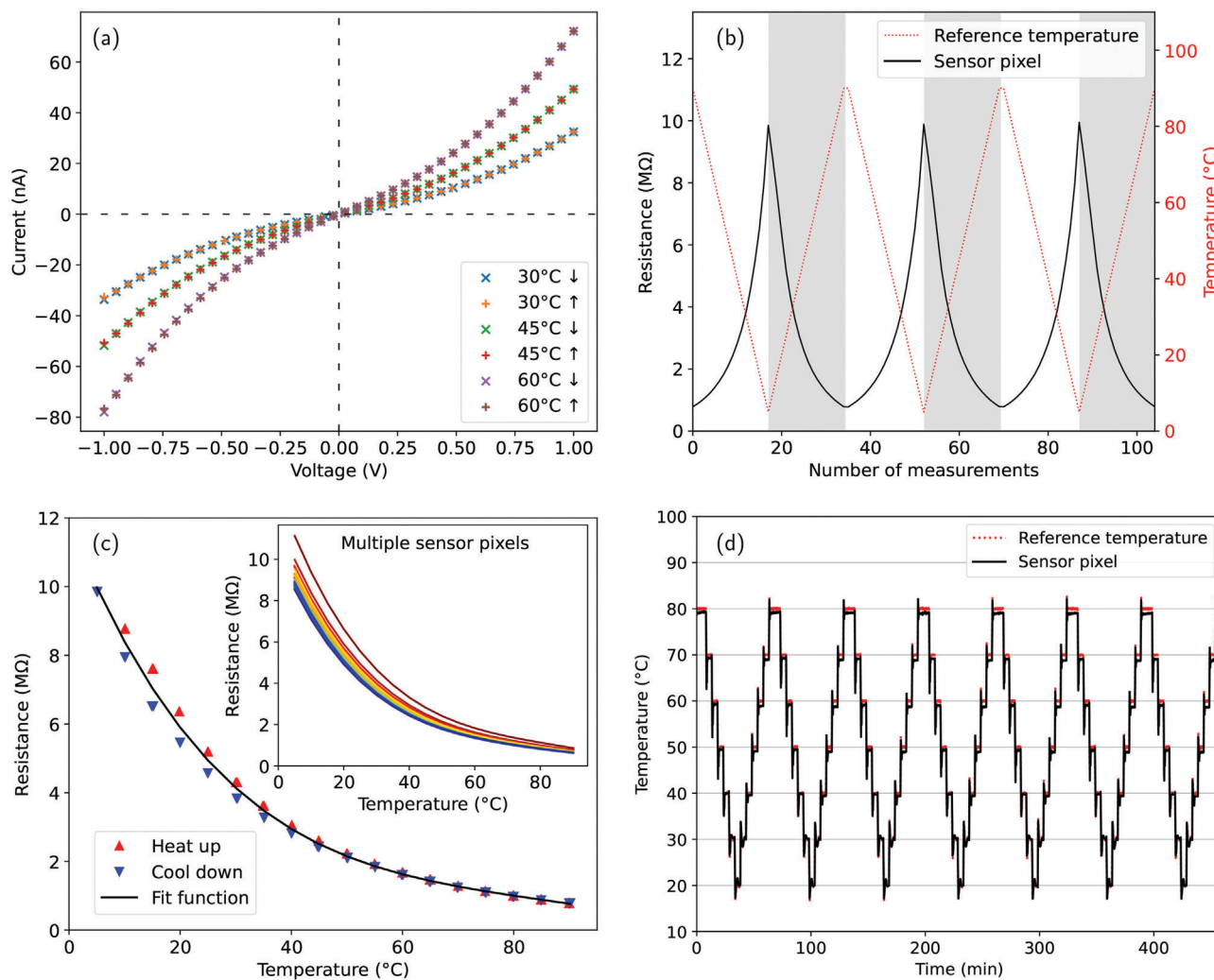
**ADVANCED**
**SCIENCE NEWS**

www.advancedsciencenews.com

**ADVANCED**
**SENSOR**
**RESEARCH**
Open Access

www.advsensorres.com

**Figure 2.** a) *I–V* measurement of a single pixel at different temperatures. The voltage is swept from −1 to +1 V and back again without revealing any hysteresis or charge effects. The arrows depict the sweeping direction. The non-linear behavior is typical for a NTC material and is perfectly symmetrical around 0 V, which is to be expected from the symmetric sensor stack. b) Temperature cycle between 5 and 90 °C while recording the resistance if the sensor pixels. The sensor response is repeatable and stable, but also shows the non-linear behavior of the thermistor material. c) Taking the temperature response of each pixel and correlating it with the reference temperature, individual calibration functions can be calculated. A small hysteresis effect develops between the heating and cooling phase during temperature cycling at lower temperatures. The inlet plot shows the behavior for multiple sensor pixels. d) The calibration functions are tested by comparing the calculated temperature of the sensor pixel with the reference temperature. Therefore, the sensor has to undergo several temperature cycles between 20 and 80 °C. More detailed plots can be found in the Figure S4 (Supporting Information).

small drift in resistance corresponding to a temperature variation of <2.5 °C. The effect is partly reversible and depends on the previous temperature history. This drift can potentially be attributed to the above mentioned relaxation mechanism in the polymer's matrix. To demonstrate the calibration and the stability of the sensor stack, Figure 2d shows the temperature reading of one single sensor tested against the commercial reference temperature sensor. Even after multiple iterations we could not observe any drift in the sensor response. A small hysteresis effect was observed above 50 °C. Similar to the calibration, the strength of the effect was influenced depending on the present tempering phase. More details extracted from Figure 2d are presented in Figure S4 (Supporting Information). For each temperature step, the measurement setup generates a temperature overshoot, which is also ev-

ident in the spikes at each step. The printed sensor shows a fast response and is able to fully resolve the temperature overshoot depicted in the measurement curve. This is not always the case for the reference sensor due to a low sampling rate of several 100 ms from the commercial reference sensor based on a Pt100.

Reading the sensor array with the measurement setup (**Figure 3**a) follows a certain sequence: First, by switching row and column with the multiplexing unit, one sensor pixel is addressed. Next, the resistance value is recorded with the SMU and saved to the buffer. These two alternating operations are repeated until the complete sensor is read out. Right after, the data is transferred to the PC and the values are interpreted with the corresponding fitting function for each pixel. The temperature distribution over the sensor is visualized in a 2D thermal map
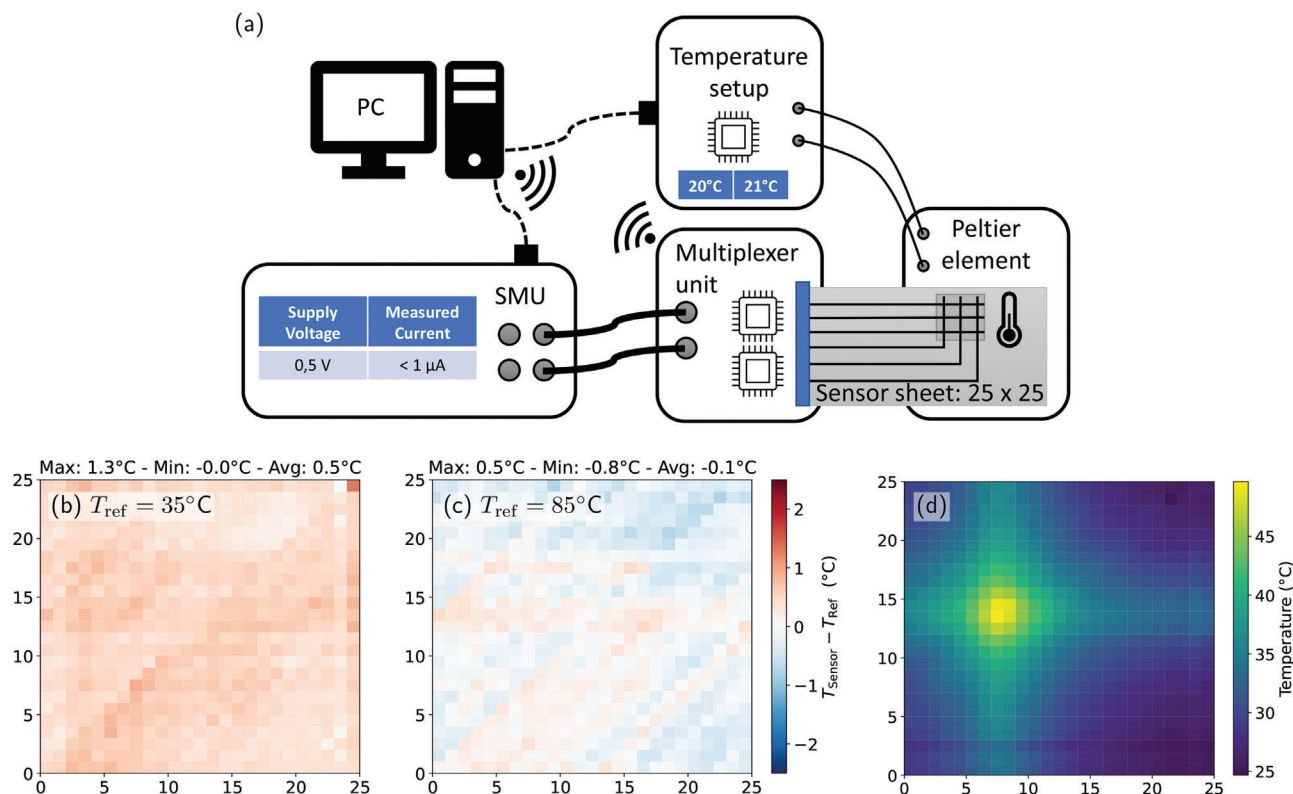
**ADVANCED
SCIENCE NEWS**

www.advancedsciencenews.com

**ADVANCED
SENSOR
RESEARCH**
Open Access

www.advsensorres.com

**Figure 3.** a) All measurements presented in Figure 2 were conducted on the depicted setup. It consists of a SMU, a multiplexing device to which the sensor is attached to and a temperature setup including a peltier-based heating/cooling unit. Each device is managed by a Raspberry Pi. For the measurement the SMU was set to supply a fixed voltage of 0.5 V. b,c) Evaluating the calibration process for the entire sensor array at different reference temperatures ($T_{ref}$). d) Temperature sensor array image of a heated solder tip in direct contact with the sensor array to demonstrate the thermal imaging capabilities.

as shown in **Figure 4**b. The image resolution is defined by the number of pixels of the sensor array. To test the calibration for all sensor pixels simultaneously the entire sensor array is uniformly heated. The deviation between reference temperature and interpreted temperature is displayed in Figure 3b,c. For a stabilized temperature, we observed a maximum average deviation of ±0.5 °C with individual sensor pixels showing a deviation of up to ±1.3 °C in the presented images. Presumably, the measurement is affected by several influences, such as the observed hysteresis effect, switching and measuring effects of the multiplexing circuitry and electromagnetic interference from the environment. To demonstrate the full functionality of the sensor array, it is necessary to demonstrate that the array is also able to display a local heat source. Therefore, we used a 22 mW green laser mounted above the sensor array. The sensor sheet is turned upside down, so that the laser is heating up the sensor stack through the substrate. An ultra thin, black, non-transparent tape is added to the back side of the substrate to increase the absorption and prevent potential charge induction by photons. This ensures that the measured resistance change is exclusively caused by a temperature change. Figure 4a,b and Figure S6 (Supporting Information) display the resulting thermal images caused by the illumination. In both images the localized laser spot is clearly visible. To verify the temperature distribution measured with the printed sensor and represented as 2D or 3D thermal map (Figure 4b; Figure S5, Supporting Information), we compared the result to a thermographic image of the sensor surface (Figure 4a).

In the figures, two ridges are visible, running along the electrodes in horizontal and vertical direction, each originating from the central hot spot. To investigate this effect, several thermographic images of the laser spot on the sensor array are taken (Figure S6, Supporting Information) and recorded from the front side. The images unveil the different heat conduction properties of the utilized materials. Due to the worse heat conduction of the PEN substrate the heat distribution is limited to a smaller area and in return the substrate reaches locally higher temperatures. In contrast, the better heat conduction properties of the silver electrodes causes a increased heat distribution horizontal and vertical direction leading to a net heat flow away from the central spot. Since, the pixels are defined by the intersecting electrodes, the heat conduction properties also influence the final temperature result. Taking these considerations into account, the observed ridges can be attributed to the heat distribution of the silver electrodes. Additionally, a minor influence from the passive matrix acting as a resistive network cannot be completely ruled out. When comparing both images, the appearance and size of the hotspot stand in good agreement. For further investigation, we placed a 100 °C hot solder tip on the backside of the sensor array (Figure 3d). It has to be mentioned that the substrate between solder tip and sensor introduces an additional isolation layer. This
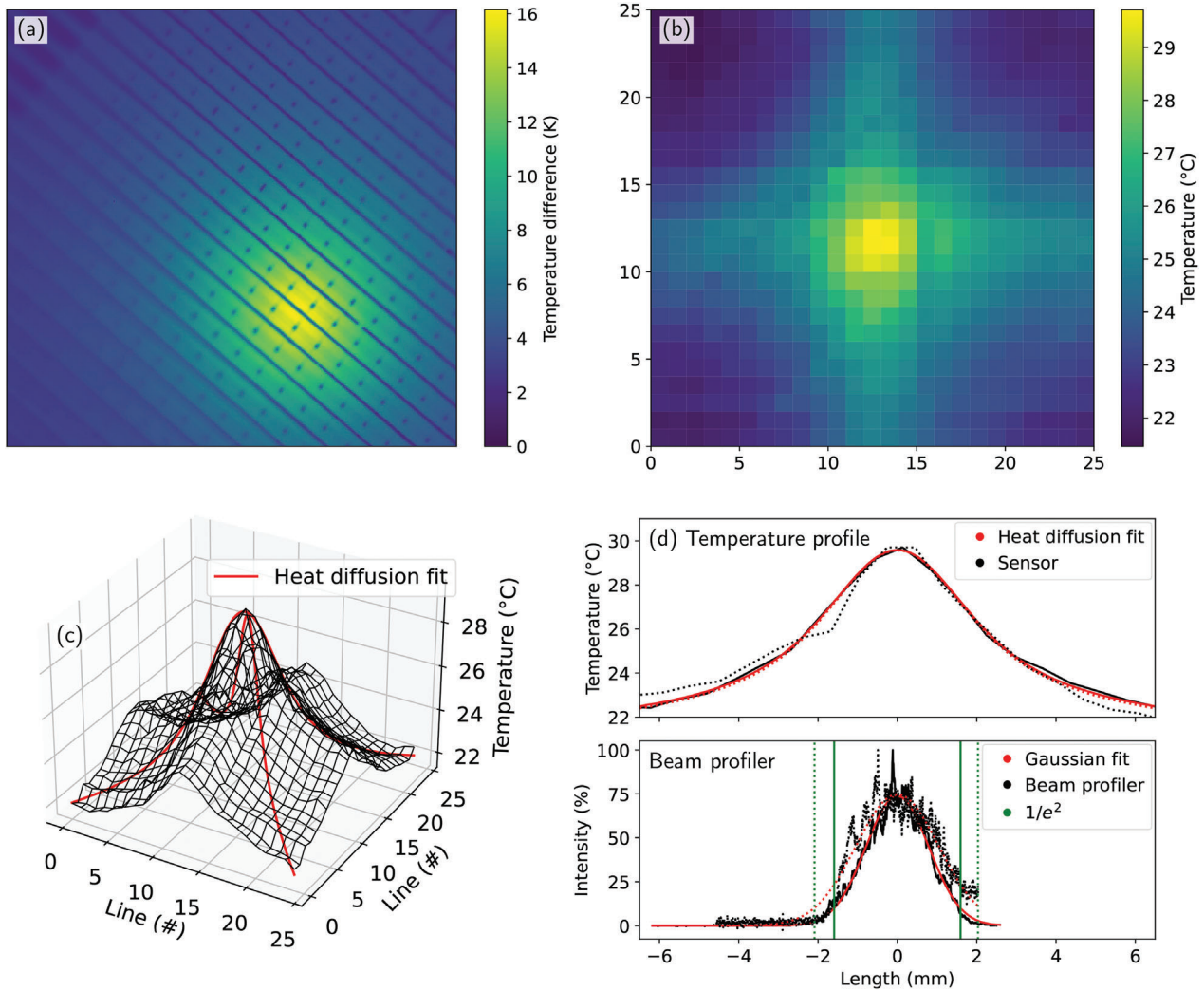
**ADVANCED
SCIENCE NEWS**

www.advancedsciencenews.com

**ADVANCED
SENSOR
RESEARCH**
Open Access

www.advsensorres.com

**Figure 4.** Measurement of a laser beam directed onto the temperature sensor. a) Thermal image of the heat distribution of a local hot spot induced by a laser beam recorded on an infrared camera. b) Measurement of the sensor array represented as 2D thermal map in comparison to the infrared image. c) Two diagonal cuts through the temperature profile were used and extracted to determine the beam profile. Each profile was evaluated by a Gaussian fit (red). d) Comparison between observed temperature profile with the sensor sheet and beam profile measured with a beam profiler. The temperature distribution is fitted according to Equation 3.

and the described heat distribution have to be considered for the measurement. In general, both local heat sources generate a similar sensor response proving that the observed effects are not heat source related but have to be attributed to the sensor.

Each square visible in Figure 4a,b corresponds to a pixel pitch area of 500×500 μm$^2$, which comprises one central sensor pixel of with a size of 60×60 μm$^2$. The sensor resolution is sufficient to determine beam properties such as the beam diameter. Since we observed the ridges in vertical and horizontal direction, we decided to take the measurement data along the diagonals. Both diagonal cuts cross at the temperature peak corresponding to the center of the laser beam, as shown in Figure 4c. From the measurement data, two datasets according to the diagonal cuts are extracted. To derive the beam diameter from the measurement, the inhomogeneous heat equation for the steady state was solved

$$-\alpha \nabla^2 T(r) = f(r) \tag{1}$$

where $\alpha$ represents the thermal diffusivity. For this work, we consider a constant Gaussian beam profile, which defines the source term $f(r)$

$$f(r) = A \cdot \exp\left(\frac{-r^2}{\sqrt{2\omega^2}}\right) \tag{2}$$

The laser waist $\omega$ and the amplitude $A$ characterize the beam profile. Due to the rotational symmetry of the discussed problem, the equation can be solved using the Laplacian in polar coordinates

$$T(r) = \widetilde{A}_\alpha \omega^3 \frac{\sqrt{2\pi}}{2} \frac{1}{r} \cdot \text{erf}\left(\frac{r}{\sqrt{2\omega^2}}\right) \tag{3}$$

For simplification, we combine $\frac{A}{\alpha} = \widetilde{A}_\alpha$. Subsequently, the datasets are fitted individually with Equation 3, resulting in great

**ADVANCED
SCIENCE NEWS**

www.advancedsciencenews.com

**ADVANCED
SENSOR
RESEARCH**
Open Access

www.advsensorres.com

agreement with the measurement curves. With the retrieved fit parameters, we determine the initial source term (Equation 2), representing the used laser beam. From this parameterized Gaussian beam distribution we then calculate the beam diameter (two times the radius where the intensity has dropped to $1/e^2$). Figure 4d shows both diagonal cuts from the measured temperature profiles recorded with the temperature sensor array and fitted with the associated heat diffusion equation. As described, we derive the initial beam diameter from the parameters, which leads to a diameter of $D = 4.42 \pm 0.03$ mm. For comparison, the beam properties (Figure 4d) were also measured with a beam profiler (BC106N-VIS/M - CCD Camera Beam Profiler, Thorlabs, Inc.), resulting in a beam diameter of $D_{profiler} = 3.85 \pm 0.27$ mm. Therefore, we observed only a deviation of less than 14 % between both measurement methods. The difference can be attributed to the inhomogeneous temperature distribution over the sensor due to the deposited layers and different material properties, as well as a mutual influence by neighboring sensor pixels. Also, the laser absorption properties and potential cooling effects by convection or radiation stay unconsidered in the equation. Eventually, this effect can be accounted for by introducing a calibration function. Leaving the ridges in horizontal and vertical direction aside, the beam profile appears symmetrical, which is also reflected in a matching heat diffusion fits and the beam representation in the thermographic image. We also challenged the spatial resolution of the temperature sensor array by investigating two overlapping laser spots. For laser spots with a spacing of 2 mm and more the sensor array was able to resolve two individual heat sources (Figure S7, Supporting Information).

## 4. Conclusion

We demonstrated a fully printed temperature sensor on a flexible substrate with high spatial resolution. The fabrication involves screen printing for the connection lines and aerosol jet printing for the actual sensor stack. Despite the size of only 12×12 mm², the sensor array comprises a total of 625 sensor pixels. Comparing the demonstrated temperature sensor array with published state-of-the-art devices (Table 1), our sensor density and fabrication size is superior. This is accompanied by a significant spatial thermal resolution improvement. The used thermistor material is commercially available, but was partially customized to ensure printability. It exhibits a NTC and shows a non-linear behavior with a strong temperature dependency of up to 3.6 % °C⁻¹. Since the sensor has proven to be robust against external influences, we could avoid encapsulation. The layout is based on a passive matrix with 25 by 25 lines, all individually addressed by an attachable multiplexing unit connected to a resistance measurement system. Each pixel is calibrated individually leading to an average temperature deviation across the sensor array of <0.5 °C. Utilizing a laser to locally induce heat in the temperature array, we are able to determine the beam diameter from solving the heat diffusion equation. This demonstrates an interesting application case for the detection of infrared radiation, especially in the mid and far infrared range. To further increase temperature resolution and readout speed, it would be advantageous to develop the multiplexer unit into fully integrated readout electronics. In conclusion, the fabrication route of the sensor demonstrates the great potential of digital printing technologies combining large area and high precision printing on flexible substrates or directly integrated in an additive manufacturing process.

## 5. Experimental Section

*Array Fabrication*:    The complete fabrication of the temperature sensor array was carried out in a hybrid process using a screen printer followed by aerosol jet printing of the sensor stack. The process flow is depicted in Figure 1a. All sensors were printed on a 100 µm-thick PEN substrates, which were rinsed with 2-propanol and dried with an air gun prior to the printing process. First, the connection lines were printed on a semi-automatic screen printing machine (RokuPrint SD05). A screen fineness of 165 threads cm⁻¹ (420 threads inch⁻¹) with a thread diameter of 27 µm was used for the deposition of the commercially available silver paste (LOCTITE ECI 1010 E&C, Henkel,34). After printing, the silver layer was cured on a hotplate at 120 °C for 15 min. Each silver line has a width of 300 µm with a layer thickness of <3 µm measured on a stylus profiling system (Profilometer, DektakXT, Bruker) resulting in a resistance of <2 Ω per 10 mm length (See also Figures S1 and S9, Supporting Information). Next, the sensor stack was printed on an aerosol jet printer (Aerosol Jet 5X System, Optomec, Inc.). That required three subsequent printing/curing steps: 1) Bottom electrode 2) Thermistor material 3) Top electrode. The bottom electrode was printed using a water based silver ink from Novacentrix (JS-A221AE,33), which was compatible to the ultrasonic atomizer (UA) cassette requiring 3 mL of ink. For deposition, a 150 µm nozzle with an atomizer flow rate of 22 sccm and a sheath gas flow rate of 50 sccm were used. The printer exhibited a solvent add-back, which was filled with deionized-water and heated to 28 °C. The ink tank was operated with a sonication power settings of 400–420 mA for mist generation at 27 °C. With a printing speed of 10 mm s⁻¹ an electrode width of ≈55–70 µm and a thickness of <4 µm was achieved. The silver layer was sintered on a flash sintering system (Pulseforge 1200, Novacentrix), immediately after finishing the feature on the aerosol jet. The bottom electrode was sintered with a lamp driver voltage of 420 V for 200 µs, 75 repetitions and a rate of 2 Hz. The parameters were optimized to achieve a highly conductive and crack free result. The aerosol jetted silver electrodes were printed on top of the screen printed connection lines, which led to an overlapping region where both silver lines were in direct contact (Figure S6a,d, Supporting Information). Next, the thermistor material was printed perpendicular over the bottom electrode. The sensor pixel uniformity was significantly influenced by the homogeneity of the thermistor layer. It was found that the atomizer stream was slightly affected when the shutter was operated due to pressure variations in the system. Even though, the effect was small, a gradient in the measured resistance values was observed. Therefore, a mask that was placed on top of the sensor with an opening at the location of the sensor stack was used. That allowed to print the 25 lines in one continuous meander structure and remove the structure outside the defined area by simply lifting the mask. The commercially available dielectric screen printing ink (LOCTITE EDAG PM 404 E&C, Henkel AG & Co. KGaA,35) was adapted to be used on the aerosol jet printer. To prepare the ink, 9 g of LOCTITE EDAG PM 404 E&C was diluted with 4.5 mL triethylene glycol monomethyl ether (TGME) and thoroughly mixed with a vortex mixer. With this process, the viscosity was lowered to $\eta = 2100$ mPa·s (cP) at a shear rate of $\gamma = 1.5$ s⁻¹ from initially $\eta = 10000 - 20000$ mPa·s (cP).35 The ink viscosity was determined by a rheometric measurement (Haake Mars Modular Advanced Rheometer System, Thermo Fisher Scientific).The ink had to form a viscous honey-like fluid. The ink properties required a pneumatic atomizer (PA) cassette and 10 mL of ink fluid. As soon as the ink was filled into the ink tank, it was important to run the integrated stirrer at 5 V to avoid agglomeration and clogging of the atomizer orifice. Furthermore, it proved beneficial to heat the ink tank to 28 °C. The PA cassette also included a solvent add-back, which was filled with 2-propanol and heated to 25 °C. The printing was conducted with a 600 µm nozzle, featuring an atomizer flow rate of 1200 sccm, a sheath flow rate of 250 sccm, a virtual impactor sheath gas flow rate of 1200 sccm, and a virtual impactor exhaust pressure of 0.1 psi. It was important to avoid build-up of excessive ink on the substrate because the nozzle jet would

**ADVANCED
SCIENCE NEWS**

www.advancedsciencenews.com

**ADVANCED
SENSOR
RESEARCH**

www.advsensorres.com

blow the ink droplets to the side, leading to unwanted layer thicknesses. For better control, it was preferable to print wide lines instead of a closed thermistor layer (Figure S9a–c, Supporting Information). Twelve thermistor layers with a printing speed of 10 mm s$^{-1}$ were printed. These 12 layers add up to a thickness of ≈3–4 μm (Figures S1 and S9c, Supporting Information) in the center and a line width of >450 μm. After printing, the substrate was placed in an oven (UF55plus, Memmert GmbH + Co. KG) at 120 °C for at least 6 h. Finally, the top electrode was printed on top in the center of the thermistor layers. Following the printing direction of the underlying thermistor lines led to the best results in terms of resistance uniformity and print/curing quality. The aerosol jet printing parameters were similar to the parameters employed for the bottom electrode. Due to the underlying thermistor material, the achieved line width was reduced to >45 μm, which required adapted curing parameters for photonic sintering. The lamp driver voltage was increased to 480 V for 160 μs with 150 repetitions and a rate of 1 Hz. In a last final step, the sensor sheet was heated to 120 °C for 24 h in order to let the material settle and prevent drifting. The total layer thickness of one sensor pixel was ≈<12.3 μm comprising two layers of aerosol jet silver and the sandwiched thermistor layer.

*Characterization*: A schematic of the complete readout and evaluation setup is shown in Figure 3a. For characterization the sensor sheet was mounted in a specially designed multiplexing unit. The connection between sensor sheet and printed-circuit-board (PCB) was established with FPC connectors (Würth Elektronik eiSos GmbH & Co. KG), which required a matching connection line layout. The multiplexing unit was compatible with 4-terminal measurement and features four 32:1 channel multiplexers (ADG731BSUZ, Analog Devices), which were addressed with an Arduino Nano 33 IoT. To reduce electronic noise, the PCB was powered by a powerbank and got controlled wireless. The sensor signal was forwarded to a SMU (2450 SourceMeter ®; SMU Instrument, Tektronix, Inc.) sourcing a fixed voltage of 0.5 V and measuring the current. For calibration and temperature cycling, the sensor was mounted into a self-built proportional-integral-derivative (PID)-controlled temperature setup. The sensor was placed between an insulating layer of foamed polystyrene and a peltier element (QC-241-1.0-3.0M, Quick-Ohm Küpper & Co. GmbH). The setup automatically adjusted temperature to a defined value in the range from 0 to 90 °C by both heating and cooling. An embedded Pt100 temperature sensor served as reference sensor. All devices were controlled by a Raspberry Pi 4 running a Python 3 script. The script featured a calibration mode and several measurement modes. When reading the sensor array, the measurement followed a default sequence. First, a certain pixel was requested from the multiplexing unit. As soon as the switching process was confirmed, the current measurement was triggered on the SMU. After all pixels of the array were read out, the measurement values were transferred from the SMU and temperature setup to the Raspberry Pi. The data were processed and got stored. Then, a new cycle started acquiring the data for a new frame. To reduce the mutual influence among the pixels during the measurement, switching in a manner that always row and column is switched was implemented. That led to a diagonal readout of the sensor sheet. The frame rate was limited by the switching speed and the sampling rate of the SMU, adding up to ≈2 min to measure all 625 sensor pixels.

## Supporting Information

Supporting Information is available from the Wiley Online Library or from the author.

## Conflict of Interest

The authors declare no conflict of interest.

## Data Availability Statement

The data that support the findings of this study are available from the corresponding author upon reasonable request.

[1] K. Xu, Y. Lu, K. Takei, *Adv. Mater. Technol.* **2019**, *4*, 1800628.

[2] L. V. Kayser, D. J. Lipomi, *Adv. Mater.* **2019**, *31*, 10.

[3] A. Koivikko, E. S. Raei, M. Mosallaei, M. Mäntysalo, V. Sariola, *IEEE Sens. J.* **2018**, *18*, 223.

[4] D. Katerinopoulou, P. Zalar, J. Sweelssen, G. Kiriakidis, C. Rentrop, P. Groen, G. H. Gelinck, J. van den Brand, E. C. P. Smits, *Adv. Electron. Mater.* **2019**, *5*, 1800605.

[5] Y. F. Wang, T. Sekine, Y. Takeda, K. Yokosawa, H. Matsui, D. Kumaki, T. Shiba, T. Nishikawa, S. Tokito, *Sci. Rep.* **2020**, *10*, 1.

[6] S. Han, J. Kim, S. M. Won, Y. Ma, D. Kang, Z. Xie, K. T. Lee, H. U. Chung, A. Banks, S. Min, S. Y. Heo, C. R. Davies, J. W. Lee, C. H. Lee, B. H. Kim, K. Li, Y. Zhou, C. Wei, X. Feng, Y. Huang, J. A. Rogers, *Sci. Transl. Med.* **2018**, *10*, 435.

[7] T. Q. Trung, N. E. Lee, *Adv. Mater.* **2016**, *28*, 4338.

[8] A. Tarancon, V. Esposito, M. T. Faro, M. D. Vece, J. S. Son, P. Norby, S. Bag, P. S. Grant, A. Vogelpoth, S. Linnenbrink, M. Brucki, T. Schophoven, A. Gasser, E. Persembe, D. Koufou, S. Kuhn, R. Ameloot, X. Hou, K. Engelbrecht, C. R. H. Bahl, N. Pryds, J. Wang, C. Tsouris, E. Miramontes, L. Love, C. Lai, X. Sun, M. R. Kærn, G. Criscuolo, D. B. Pedersen, *Journal of Physics: Energy* **2022**.

[9] S. Lanceros-Méndez, C. M. Costa, *Printed Batteries* **2018**.

[10] Z. Cui, *Printed Electronics*, Wiley, Singapore **2016**.

[11] V. Kantola, J. Kulovesi, L. Lahti, R. Lin, M. Zavodchikova, E. Coatanéa, *Printed Electronics, Now and Future*, **2009**.

[12] D. Maddipatla, B. B. Narakathu, M. Atashbar, *Biosensors* **2020**, *10*, 12.

[13] T. Vuorinen, J. Niittynen, T. Kankkunen, T. M. Kraft, M. Mäntysalo, *Sci. Rep.* **2016**, *6*, 35289.

[14] S. Harada, W. Honda, T. Arie, S. Akita, K. Takei **2014**.

[15] K. Kanao, S. Harada, Y. Yamamoto, W. Honda, T. Arie, S. Akita, K. Takei, *RSC Adv.* **2015**, *5*, 30170.

[16] S. Khan, L. Lorenzelli, R. S. Dahiya, *IEEE Sens. J.* **2015**, *15*, 3164.

[17] M. T. Rahman, C.-Y. Cheng, B. Karagoz, M. Renn, M. Schrandt, A. Gellman, R. Panat, *ACS Appl. Nano Mater.* **2019**, *2*, 3280.

[18] C. Offenzeller, M. Knoll, T. Voglhuber-Brunnmaier, M. A. Hintermuller, B. Jakoby, W. Hilber, *IEEE Sens. J.* **2018**, *18*, 8685.

[19] S. Duby, B. Ramsey, D. Harrison, G. Hay, *Proceedings of IEEE Sensors* **2004**, *3*, 1098.

[20] Q. Li, L. Zhang, X. Tao, X. Ding, *Adv. Healthcare Mater.* **2017**, *6*, 1601371.

[21] M. D. Dankoco, G. Y. Tesfay, E. Benevent, M. Bendahan, *Materials Science and Engineering B: Solid-State Materials for Advanced Technology* **2016**, *205*, 1.

[22] C. Y. Lee, G. W. Wu, W. J. Hsieh, *Sens. Actuators, A* **2008**, *147*, 173.

[23] A. Aliane, V. Fischer, M. Galliari, L. Tournon, R. Gwoziecki, C. Serbutoviez, I. Chartier, R. Coppard, *Microelectronics Journal* **2014**, *45*, 1621.

[24] X. Ren, K. Pei, B. Peng, Z. Zhang, Z. Wang, X. Wang, P. K. L. Chan, *Adv. Mater.* **2016**, *28*, 4832.

[25] R. S. Dahiya, G. Metta, M. Valle, G. Sandini, *IEEE Transactions on Robotics* **2010**, *26*, 1.

[26] T. Bücher, R. Huber, C. Eschenbaum, A. Mertens, U. Lemmer, H. Amrouch, *Scientific Reports 2022 12:1* **2022**, *12*, 1.

[27] S. Harada, K. Kanao, Y. Yamamoto, T. Arie, S. Akita, K. Takei, *ACS Nano* **2014**, *8*, 12851.

[28] Y. Xiao, S. Jiang, Y. Li, W. Zhang, *Smart Mater. Struct.* **2021**, *30*, 025035.

[29] K. Kim, M. Jung, B. Kim, J. Kim, K. Shin, O. S. Kwon, S. Jeon, *Nano Energy* **2017**, *41*, 301.

[30] I. Y. Han, S. J. Kim, *Sens. Actuators, A* **2008**, *141*, 52.

[31] T. Yokotaa, Y. Inouea, Y. Terakawaa, J. Reedera, M. Kaltenbrunnera, T. Wared, K. Yange, K. Mabuchif, T. Murakawag, M. Sekinoa, W. Voitc, T. Sekitania, T. Someyaa, *Proc. Natl. Acad. Sci. USA* **2015**, *112*, 14533.

[32] W. P. Shih, L. C. Tsao, C. W. Lee, M. Y. Cheng, C. Chang, Y. J. Yang, K. C. Fan, *Sensors* **2010**, *10*, 3597.

[33] NovaCentrix, Metalon Conductive Inks for Printed Electronics - Metalon JS-A221AE, **2011**, https://www.novacentrix.com/product/js-a221ae-silver-nanoparticles/.

[34] L. Henkel AG & Co.KGaA, TDS LOCTITE ECI 1010 E&C, March-2018, **2018**, www.henkel.com/electronics.

[35] L. Henkel AG & Co.KGaA, TDS LOCTITE EDAG PM 404 E&C, **2014**, www.henkel.com/electronics.

[36] S. A. Sergienko, *Mekhanika Kompozitnykh Materialov* **1995**, *31*, 526.

[37] C. Phillips, A. Al-Ahmadi, S. J. Potts, T. Claypole, D. Deganello, *J. Mater. Sci.* **2017**, *52*, 9520.

[38] A. Voet, *Rubber Chem. Technol.* **1981**, *54*, 42.

[39] C. Zhang, C. A. Ma, P. Wang, M. Sumita, *Carbon* **2005**, *43*, 2544.

[40] Y. Song, Q. Zheng, *Compos. Sci. Technol.* **2006**, *66*, 907.

[41] J. Feng, C. M. Chan, *Polymer* **2000**, *41*, 4559.

[42] M. K. Seo, K. Y. Rhee, S. J. Park, *Curr. Appl. Phys.* **2011**, *11*, 428.

**2200031 (10 of 10)**